Comparison of Numerical Modeling Approaches for Flow over a Wing with an Upstream Rotor

Ullhas Hebbar *, Farhan Gandhi †, and Onkar Sahni ‡
Center for Mobility with Vertical Lift (MOVE)
Scientific Computation Research Center (SCOREC)
Rensselaer Polytechnic Institute, Troy, NY, 12180

Efforts towards maximixing the aerodynamic performance of eVTOL aircraft have led to the integration of multiple propellers in close proximity of lifting surfaces. This work models an infinite rotor-wing unit at two angles of attack (AOA) of 8° and 12° based on the CRC-20 quad-rotor biplane developed by the US army using different turbulence modeling approaches including unsteady Reynolds-averaged Navier-Stokes (URANS), delayed detached eddy simulation (DDES) and large eddy simulation (LES) approaches. The actuator line model (ALM) is employed to represent the rotor as it captures key flow features including unsteadiness in the rotor wake while offering attractive computational cost saving and ease of implementation. Vortical structures from the rotor-wing unit are presented first. Results highlight LES's ability in resolving the complex on-wing vortical structures and their interaction with the rotor wake. Spanwise variation of boundary layer transition is observed in the upstroke and downstroke portions of the wing. In addition, averaged results are presented for power, thrust and sectional wing forces from different modeling approaches at 12° AOA. Significant differences are seen in sectional forces.

I. Introduction

Recent advances in the field of vertical take-off and landing (VTOL) technology as well as accompanying developments in electric storage and propulsion technologies have allowed for the advent of electric VTOL (eVTOL) aircraft; however relatively low energy densities associated with electric batteries compared to conventional hydrocarbons necessitates the maximization of aerodynamic performance. In an effort to accelerate developments in the unmanned aerial systems (UAS) domain, the US Army has recently developed common research configurations (CRCs) as a means to collaborate with researchers [1]. One such platform is the 20 lb. gross weight quadrotor bi-plane concept termed CRC-20, which is the focus of this work.

The interaction of multiple propellers and lifting surfaces in close proximity leads to complex aerodynamic interactions as featured in the rotor-blown wing CRC-20 concept. Computational studies available in the literature make a wide range of choices and assumptions for the physical modeling of such problems: different approaches to approximating the solution to the Navier-Stokes system of equations; different turbulence closure models as well as differing treatments/models for the propellers. One approach resolves the geometry of the rotor blades and accounts for blade rotation either with a sliding mesh interface or overset mesh. Another common approach models the rotors using an actuator disk/line model (ADM/ALM) where momentum sources or fictitious loads are applied in a steady or unsteady fashion to reduce the simulation cost. Aref *et al.* [2] studied both single and dual propeller blown wing configurations using a delayed detached eddy simulation (DDES) formulation and a blade resolved rotor modeled using an overset grid. Rotor-induced upwash leads to local increases in lift on the wing as well as delay in flow separation and local stall over the wing downstream of the propellers. Fischer *et al.* [3] studied the interaction of multiple propellers (up to 16) with a wing in different configurations including over-the-wing and leading edge mounted propellers. Unsteady Reynolds averaged Navier-Stokes (URANS) was used along with ALM for the rotor blades. Up to 50% increases in lift was observed with adjacent counter-rotating rotors showing the highest gains, particularly when used in the over-wing configuration. Similarly, Misiorowski *et al.* [4] studied the same CRC-20 concept used in the current study with a DDES formulation and a blade resolved propeller mesh using an overset approach. The effect of the wing on the rotor

*PhD Student, Department of Mechanical, Aerospace, and Nuclear Engineering, RPI
†Professor and Rosalind and John J. Redfern Jr. '33 Endowed Chair in Aerospace Engineering, Department of Mechanical, Aerospace and Nuclear Engineering, RPI, and AIAA Fellow
‡Associate Professor, Department of Mechanical, Aerospace, and Nuclear Engineering, RPI, and AIAA Senior Member

performance was found to be minor while ~ 20% increase in wing lift was observed compared to the isolated wing. Rotor RPM was also varied and found to dramatically affect the lift with 100% increase seen at RPM of 2x compared to baseline. Additionally, several papers [5–7] have focused on wingtip-mounted propellers where although lift generated is lower than the inboard configuration, there is a significantly smaller drag penalty, i.e., when the propeller counteracts the wingtip vortex.

This work focuses on the ALM approach due to its attractive computational cost, ease of implementation and capability to accurately capture the key flow features including unsteadiness of the rotor wake. The latter is crucial to accurately predict the aerodynamic performance of the wing with an upstream rotor. Note that the ADM approach is even more attractive from a computational viewpoint [8], however, it does not allow the capture of unsteadiness in the rotor wake. The objective of this work is to compare different turbulence modeling approaches including URANS, DDES and LES for the rotor-wing problem to predict and analyze rotor performance as well as wing-related phenomena resulting from rotor-wing interaction. This paper considers a single infinite co-rotating propeller-wing configuration based on the CRC-20 biplane at two angles of attack of 8° and 12°. Comparison from different turbulence modeling approaches is done for higher AOA of 12°. URANS and DDES approaches are well documented in previous studies and thus, we only provide the LES formulation used in this paper. While LES approach requires significant computational resources, it also provides the highest fidelity allowing the capture of relevant flow features such as transition to turbulence of the attached boundary layer over the wing [9, 10]. This is particularly crucial due to the expected spanwise non-uniformity in transition over blown and non-blown sections of the wing.

This paper is organized as follows. The LES formulation is discussed in Section II.A, followed by the problem setup and the ALM model for the rotor in Section II.B and Section II.C, respectively. The results of the study follow with instantaneous rotor-wing vortical structures in Section III.A and averaged quantities in Section III.B. Finally, concluding remarks are presented in Section IV.

II. Methodology

In this section, we present the LES formulation along with the different meshes used for the simulations as well as the ALM-based rotor representation.

A. LES Formulation

The strong form of the equations is given as:

$$\begin{aligned} &u_{k,k} = 0 \\ &u_{i,t} + (u_j - u_j^m)u_{i,j} = -p_{,i} + \tau^{\nu}_{ij,j} + f_i \end{aligned} \tag{1}$$

where u_i is the velocity vector, u_i^m is the mesh velocity vector, p is the pressure (scaled by the constant density), $\tau^{\nu}_{ij} = 2\nu S_{ij}$ is the symmetric (Newtonian) viscous stress tensor (scaled by the density), ν is the kinematic viscosity, $S_{ij} = 0.5(u_{i,j} + u_{j,i})$ is the strain-rate tensor, and f_i is the body force vector (per unit mass). Note that Einstein summation notation is used.

The weak form is stated as follows: find $\mathbf{u} \in \boldsymbol{\mathcal{S}}$ and $p \in \mathcal{P}$ such that

$$\begin{aligned} B(\{w_i, q\}, \{u_i, p\}; u_l^m) &= \int_{\Omega} \left[w_i(u_{i,t} + u_i u^m_{j,j}) + w_{i,j}(-u_i(u_j - u_j^m) + \tau^{\nu}_{ij} - p\delta_{ij}) - q_{,k}u_k \right] d\Omega \\ &+ \int_{\Gamma_h} \left[w_i(u_i(u_j - u_j^m) - \tau^{\nu}_{ij} + p\delta_{ij})n_j + q u_k n_k \right] d\Gamma_h \\ &= \int_{\Omega} w_i f_i d\Omega \end{aligned} \tag{2}$$

for all $\mathbf{w} \in \boldsymbol{\mathcal{W}}$ and $q \in \mathcal{P}$. $\boldsymbol{\mathcal{S}}$ and $\mathcal{P}$ are suitable trial/solution spaces and $\boldsymbol{\mathcal{W}}$ is the test/weight space. $\mathbf{w}$ and q are the weight functions for the velocity and pressure variables, respectively. Ω is the spatial domain and Γ_h is the portion of the domain the boundary with Neumann or natural boundary conditions.

The above weak form can be written concisely as: find $\boldsymbol{U} \in \boldsymbol{\mathcal{U}}$ such that

$$B(\boldsymbol{W},\boldsymbol{U};u_l^m) = (\boldsymbol{W},\boldsymbol{F}) \tag{3}$$

for all $\boldsymbol{W} = [\mathbf{w}, q]^T \in \boldsymbol{\mathcal{V}}$. $\boldsymbol{U} = [\mathbf{u}, p]^T$ is the vector of unknown solution variables and $\boldsymbol{F} = [\mathbf{f}, 0]^T$ is the source vector. The solution and weight spaces are: $\boldsymbol{\mathcal{U}} = \{\boldsymbol{U} = [\mathbf{u}, q]^T | \mathbf{u} \in \boldsymbol{\mathcal{S}}; p \in \mathcal{P}\}$ and $\boldsymbol{\mathcal{V}} = \{\boldsymbol{W} = [\mathbf{w}, q]^T | \mathbf{w} \in \boldsymbol{\mathcal{W}}; q \in \mathcal{P}\}$, respectively.

Throughout this text $B(\cdot,\cdot)$ is used to represent the semi-linear form that is linear in its first argument and $(\cdot,\cdot)$ is used to denote the L_2 inner product. $B(\boldsymbol{W},\boldsymbol{U};u_l^m)$ is split into bilinear and semi-linear terms as shown below.

$$B(\boldsymbol{W},\boldsymbol{U};u_l^m) = B_1(\boldsymbol{W},\boldsymbol{U};u_l^m) + B_2(\boldsymbol{W},\boldsymbol{U}) = (\boldsymbol{W},\boldsymbol{F}) \tag{4}$$

where $B_1(\boldsymbol{W},\boldsymbol{U};u_l^m)$ contains the bilinear terms and $B_2(\boldsymbol{W},\boldsymbol{U})$ consists of the semi-linear terms. These are defined as

$$\begin{aligned} B_1(\boldsymbol{W},\boldsymbol{U};u_l^m) = &\int_\Omega \left[w_i(u_{i,t} + u_i u_{j,j}^m) + w_{i,j}(u_i u_j^m + \tau_{ij}^\nu - p\delta_{ij}) - q_{,k}u_k\right] d\Omega \\ &+ \int_{\Gamma_h} \left[w_i(-u_i u_j^m - \tau_{ij}^\nu + p\delta_{ij})n_j + q u_k n_k\right] d\Gamma_h \end{aligned} \tag{5}$$

$$B_2(\boldsymbol{W},\boldsymbol{U}) = -\int_\Omega w_{i,j} u_i u_j d\Omega + \int_{\Gamma_h} w_i u_i u_j n_j d\Gamma_h \tag{6}$$

The Galerkin weak form is obtained by considering the finite-dimensional or discrete solution spaces $\boldsymbol{\mathcal{S}}^h \subset \boldsymbol{\mathcal{S}}$ and $\mathcal{P}^h \subset \mathcal{P}$ and the weight space $\boldsymbol{\mathcal{W}}^h \subset \boldsymbol{\mathcal{W}}$, where the superscript h is used as a mesh parameter to denote discretized spaces and variables in a finite element context. Using these spaces, $\boldsymbol{\mathcal{U}}^h = \{\boldsymbol{U}^h = [\mathbf{u}^h, p^h]^T | \mathbf{u}^h \in \boldsymbol{\mathcal{S}}^h; p^h \in \mathcal{P}^h\}$ and $\boldsymbol{\mathcal{V}}^h = \{\boldsymbol{W}^h = [\mathbf{w}^h, q^h]^T | \mathbf{w}^h \in \boldsymbol{\mathcal{W}}^h; q^h \in \mathcal{P}^h\}$ are defined. The Galerkin weak form is then stated concisely as: find $\boldsymbol{U}^h \in \boldsymbol{\mathcal{U}}^h$ such that

$$B(\boldsymbol{W}^h,\boldsymbol{U}^h) = (\boldsymbol{W}^h,\boldsymbol{F}) \tag{7}$$

for all $\boldsymbol{W}^h \in \boldsymbol{\mathcal{V}}^h$. Note for brevity we have dropped u_l^m term in the arguments of the semi-linear form. The Galerkin weak formulation corresponds to a method for direct numerical simulation since no modeling is employed. However, when the finite-dimensional spaces are incapable of representing the fine/small scales, the Galerkin formulation yields an inaccurate solution. A model term is added to overcome this difficulty, e.g., as done in the residual-based variational multiscale (RBVMS) formulation.

In RBVMS, a set of model terms is added to the Galerkin weak form that results in the following variational formulation: find $\boldsymbol{U}^h \in \boldsymbol{\mathcal{U}}^h$ such that

$$B(\boldsymbol{W}^h,\boldsymbol{U}^h) + M_{rbvms}(\boldsymbol{W}^h,\boldsymbol{U}^h) = (\boldsymbol{W}^h,\boldsymbol{F}) \tag{8}$$

for all $\boldsymbol{W}^h \in \boldsymbol{\mathcal{V}}^h$. M_{rbvms} represents the set of model terms due to the RBVMS approach.

A scale separation is used to decompose the solution and weight spaces as $\boldsymbol{\mathcal{S}} = \boldsymbol{\mathcal{S}}^h \oplus \boldsymbol{\mathcal{S}}'$ and $\mathcal{P} = \mathcal{P}^h \oplus \mathcal{P}'$, and $\boldsymbol{\mathcal{W}} = \boldsymbol{\mathcal{W}}^h \oplus \boldsymbol{\mathcal{W}}'$, respectively. Thus, the solution and weight functions are decomposed as $u_i = u_i^h + u_i'$ and $p = p^h + p'$ or $\boldsymbol{U} = \boldsymbol{U}^h + \boldsymbol{U}'$, and $w_i = w_i^h + w_i'$ and $q = q^h + q'$ or $\boldsymbol{W} = \boldsymbol{W}^h + \boldsymbol{W}'$, respectively. Note that coarse-scale or resolved quantities are denoted by $(\cdot)^h$ and fine-scale or unresolved quantities by $(\cdot)'$. The coarse-scale quantities are resolved by the grid whereas the effects of the fine scales on the coarse scales are modeled. In RBVMS, the fine scales are modeled as a function of the strong-form residual due to the coarse-scale solution. This is represented abstractly as $\boldsymbol{U}' = \mathcal{F}(\boldsymbol{R}(\boldsymbol{U}^h);\boldsymbol{U}^h)$, where $\boldsymbol{R}(\cdot) = [\boldsymbol{R}^m(\cdot), R^c(\cdot)]^T$ is the strong-form residual of the equations with $\boldsymbol{R}^m(\cdot)$ (or $R_i^m(\cdot)$) and $R^c(\cdot)$ as those of the momentum and continuity equations, respectively. Specifically, the fine-scale quantities are modeled as $u_i' \approx -\tau_M R_i^m(u_k^h, p^h; u_l^m)$ and $p' \approx -\tau_C R^c(u_k^h)$, where τ_C and τ_M are stabilization parameters (e.g., see details in Tran and Sahni [11]). This provides a closure to the coarse-scale problem as it involves coarse-scale solution as the only unknown. This is why $M_{rbvms}(\boldsymbol{W}^h,\boldsymbol{U}^h)$ is written only in terms of the unknown coarse-scale solution $\boldsymbol{U}^h$. In summary, $M_{rbvms}(\boldsymbol{W}^h,\boldsymbol{U}^h)$ can be written as

$$
\begin{aligned}
&M_{rbvms}(\boldsymbol{W}^h, \boldsymbol{U}^h) = \\
&\sum_e \int_{\Omega_e^h} [\underbrace{-(w_i^h u_{j,j}^m + w_{i,j}^h u_j^m)\tau_M R_i^m(u_k^h, p^h; u_l^m)}_{M^{ALE}_{rbvms}(\boldsymbol{W}^h,\boldsymbol{U}^h)} \\
&\quad + \underbrace{q_{,i}^h \tau_M R_i^m(u_k^h, p^h; u_l^m)}_{M^{cont}_{rbvms}(\boldsymbol{W}^h,\boldsymbol{U}^h)} + \underbrace{w_{i,j}^h \tau_C R^c(u_k^h)\delta_{ij}}_{M^{P}_{rbvms}(\boldsymbol{W}^h,\boldsymbol{U}^h)} \\
&\quad + \underbrace{w_{i,j}^h \left(u_i^h \tau_M R_j^m(u_k^h, p^h; u_l^m) + \tau_M R_i^m(u_k^h, p^h; u_l^m) u_j^h\right)}_{M^{C}_{rbvms}(\boldsymbol{W}^h,\boldsymbol{U}^h)} \\
&\quad \underbrace{-w_{i,j}^h \tau_M R_i^m(u_k^h, p^h; u_l^m)\tau_M R_j^m(u_k^h, p^h)}_{M^{R}_{rbvms}(\boldsymbol{W}^h,\boldsymbol{U}^h)}] d\Omega_e^h
\end{aligned}
\tag{9}
$$

Note that all model terms are written in terms of the resolved scales within each element (where e denotes an element and contributions from all elements are summed). The last model term is used to represent the Reynolds stresses (i.e., M^R_{rbvms}) while the two terms before it are used to represent the cross-stress terms (i.e., M^C_{rbvms}).

B. Problem Setup

The complete CRC-20 case is a quad-rotor biplane system. For this paper, half-wing unit of the CRC-20 concept with one rotor (as shown in Fig. 1) is simulated as an infinite co-rotating rotor-blown wing by making use of the periodic boundary conditions in the spanwise direction. The 60.9 cm (24 in) diameter rotor is placed at the center of the half-wing unit, and 6.98 cm (2.75 in) upstream of the leading edge of the half-wing with a span of 76.2 cm (30 in). The maximum blade chord is $c_r = 6.15$ cm. The wing itself is composed of an untapered and untwisted airfoil cross-section corresponding to the Wortmann FX 63-137 airfoil with a chord of $c_w = 25.14$ cm (9.9 in). It should be noted that the rotor axis is aligned with the chord line of the wing, and the rotor is based on a scaled up version of the straight-up imaging (SUI) endurance rotor [12]. A cruise condition is simulated at two AOA's of 8° and 12°, a freestream velocity of 12.34 m/s (24 kts) and a rotational speed of 2900 RPM for the propeller resulting in a chord-based Reynolds number $\sim 250,000$.

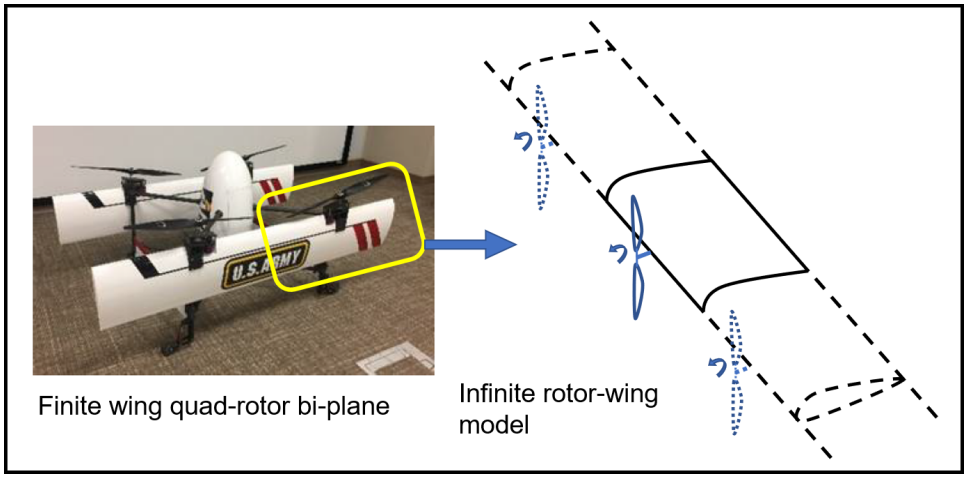

Fig. 1 CRC-20 prototype on the left side (where half-unit is highlighted) and schematic of the infinite rotor-blown wing on the right

The mesh used for the 12° ALM-LES simulation in this paper is shown in Fig. 2. A boundary layer mesh is generated over the airfoil surface with 34 layers and a first layer height corresponding to $\Delta y^+ \approx 0.5$ (at the maximum).

The span-wise and stream-wise resolutions of the boundary layer mesh is set to be up to $\Delta x^+ \approx 100$ and $\Delta z^+ \approx 50$, which are deemed appropriate for LES. In addition, several refinement zones are used. A refinement zone (R1) is defined around the rotor to properly apply ALM with a resolution of $c_r/16 \approx c_w/64$. Another refinement zone (R2) with a resolution of $c_w/128$ is defined around the wing. Finally, one more refinement zone (R3) surrounds the rotor and wing with a resolution of $c_w/32$ to sufficiently capture the wake of the rotor washing over the wing. The ALM-LES mesh contains $\sim$ 55 million elements. A similar mesh is used for the 8° ALM-LES simulation (not shown here). Fig. 3 shows the mesh used for the 12° ALM-DDES and ALM-URANS simulations. Similar to the ALM-LES mesh, a boundary layer mesh is generated over the airfoil surface with 34 layers and a first layer height corresponding to $\Delta y^+ \approx 0.5$ (at the maximum). The span-wise and stream-wise resolutions of the boundary layer mesh is set to be up to $\Delta x^+ \sim \Delta z^+ \approx 300$ which are deemed appropriate for the DDES and URANS simulations. This resolution is lower than the LES simulation as the URANS and DDES models employ RANS-based modeling near the wing. The refinement zones R1 (around rotor) and R3 (around rotor-wing unit) remain the same as the LES mesh to capture the evolution of rotor-related vorticity, while the resolution of refinement zone (R2) around the wing is set to be coarser to $c_w/64$ for the DDES and URANS simulation. This mesh contains $\sim$ 23 million elements.

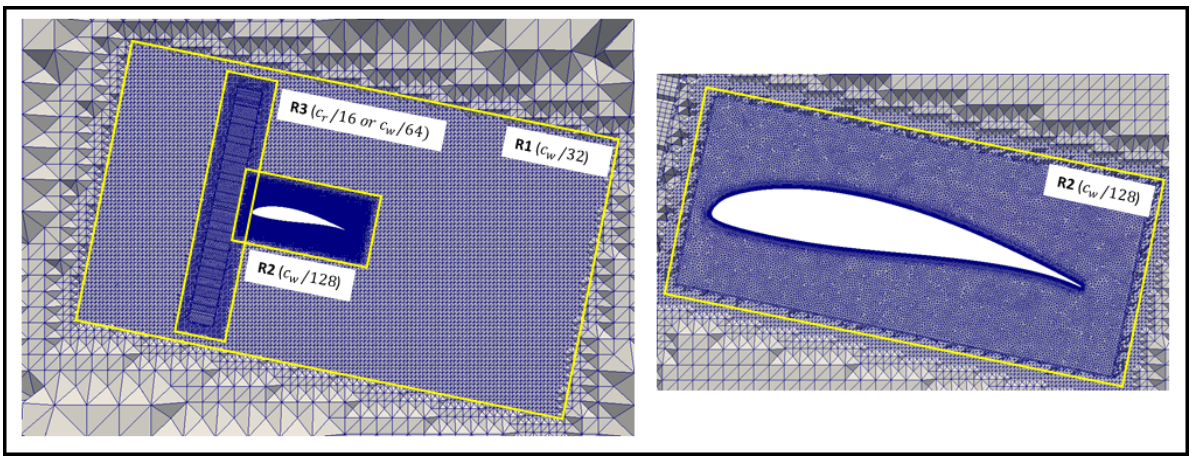

Fig. 2 Mesh used for 12° ALM-LES simulation with zoom of wing block

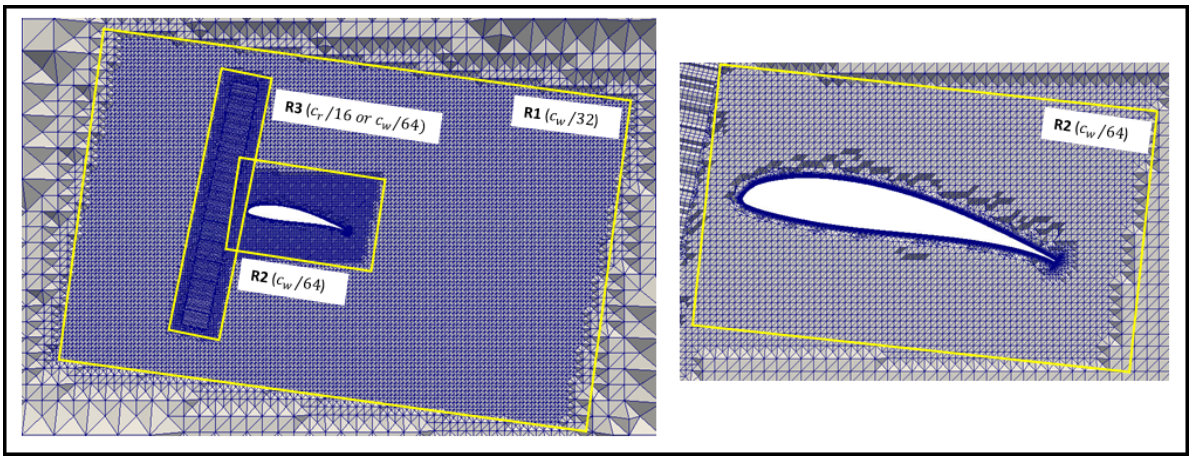

Fig. 3 Mesh used for 12° ALM-DDES simulation with zoom of wing block

A timestep corresponding to 2° rotation of the propeller is used for the second-order implicit time integration schemes employed by all simulations. Periodic conditions are used in the span, while an axial velocity of 12.34 m/s is imposed at the inlet. The outlet is located 20 chord-lengths away from the wing and set to natural pressure condition. No

penetration conditions were imposed for the upper and lower surfaces of the domain. Finally, a strong no-slip condition is imposed on the airfoil surface.

C. Rotor Model: ALM

As mentioned earlier, the propeller is modeled by imposing time-varying momentum sources in the CFD flow-field. Specifically, initial load distribution is computed from a lower-order model of Peters-He dynamic inflow using an in-house comprehensive analysis tool [13]. These loads are imposed on actuator lines representing the two-bladed rotor and are updated over the simulation based on the local flow around the rotor. Within the ALM framework, the loads over actuator lines are applied as volumetric source terms in CFD over a region defined around the actuator lines at any given instance. The width of such a region is chosen to be $\gamma = c_r$ over the entire span of the blade. Furthermore, to avoid sharp discontinuities in the load distribution, the loads are smeared in the normal and tangential directions over a width of γ [14]. In summary, the volumetric source term can be written as: $\mathbf{f_{3D}}^{CFD} = \mathbf{f_{1D}}^{BET}(r)\delta(n)\delta(\theta)$, where $f_{1D}^{BET}(r)$ is the 1D load distribution from RMAC (or loads computed from the flowfield later in the simulation), while $\delta(n)$ or $\delta(\theta)$ is a cubic spline distribution function (for $|s| \leq \gamma$) with unit area defined as (where $|s|$ is the distance of the query point from the actuator line in the tangential/normal direction):

$$\begin{cases} t_0 = \frac{s+\gamma}{\gamma}; \quad \delta(s) = \frac{1}{\gamma}\left[-2t_0^3 + 3t_0^2\right] & ; \quad s < 0 \\ t_0 = \frac{s}{\gamma}; \quad \delta(s) = \frac{1}{\gamma}\left[2t_0^3 - 3t_0^2 + 1\right] & ; \quad s \geq 0 \end{cases} \tag{10}$$

III. Results and Discussion

Vortical structures from the rotor-wing unit are presented first. Results highlight LES's ability in resolving the complex on-wing vortical structures and their interaction with the rotor wake. Spanwise variation of boundary layer transition is observed in the upstroke and downstroke portions of the wing. In addition, averaged results are presented for power, thrust and sectional wing forces from different modeling approaches at 12° AOA. Significant differences are seen in sectional forces.

A. Instantaneous Vortical Structures

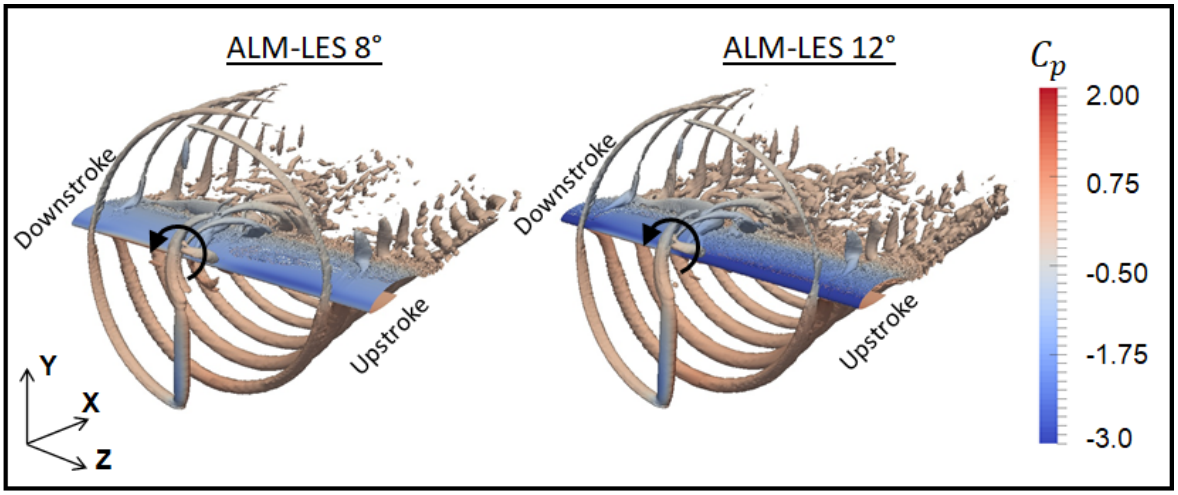

Fig. 4 Comparison of instantaneous rotor-wing vortical structures between ALM-LES 8° and 12° cases

Fig. 4 shows instantaneous views of the ALM-LES comparison between 8° and 12° cases with the rotor at the $\phi = 0°$ position (blades are vertical and rotate counterclockwise as indicated by the circular arrow), where ϕ is the azimuthal position of the rotor blades. An isosurface of Q-criterion (a qualitative indicator for vorticity and vortical

structures) is used to illustrate the complex vortical behavior involved in the rotor-blown wing problem. Coherent tip and root vortex roll-ups are visible from the rotor blades, which persist well into the rotor wake. Interestingly, there is a visible asymmetry in rotor-related vorticity below and above the wing - specifically, the thickening of the downstream tip vortices below the wing compared to the sparser vortices above, as well as the lack of blade-bound vorticity above the wing. Again, due to the proximity of the rotor and wing, there is a distinct interruption in the tip vortex evolution where the wing interferes with the rotor wake, this is visible on both the upstroke and downstroke sides of the wing. In general, the 12° case shows higher density of vortical structures, especially downstream of the wing. This is expected as the higher AOA leads to stronger shed vortices from the trailing edge. These vortices on wing also interact with the convected root and tip vortices from the rotor blades.

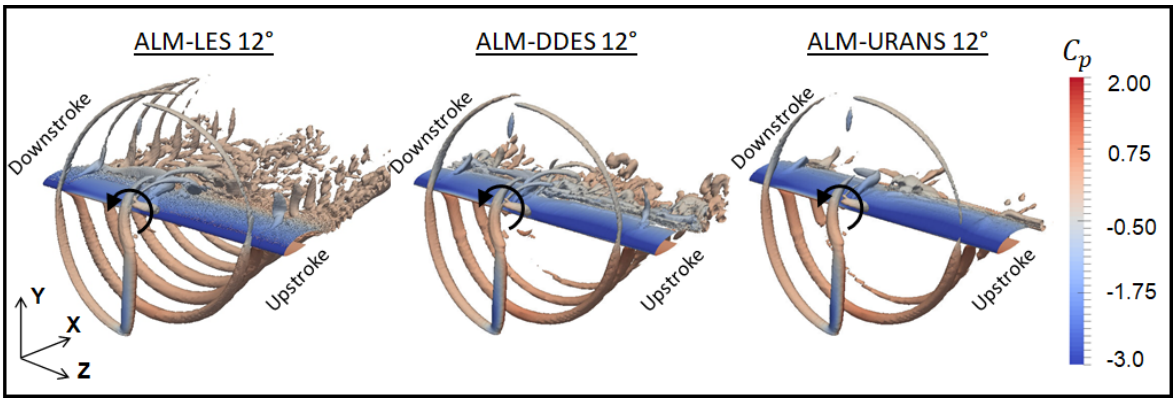

Fig. 5 Comparison of instantaneous rotor-wing vortical structures for 12° case with different turbulence models

The generated Q-criterion isosurfaces are colored with the pressure coefficient to highlight the spanwise variation in instantaneous lift generation over the wing. The upstroke side of the wing (region blown by the upstroke of the rotor) shows a significant region of lower pressure near the leading edge in both simulations. This feature has been reported in prior studies [2, 4] and is a result of the effective increase in AOA induced by the rotor upwash over the upstroke side of the wing. Although the imparted rotor thrust is higher on the downstroke side of the wing, the generated lift is lower than the upstroke side due to the induced downwash on the wing. Overall, the 12° case shows generally lower pressure (or higher lift) as compared to the 8° case.

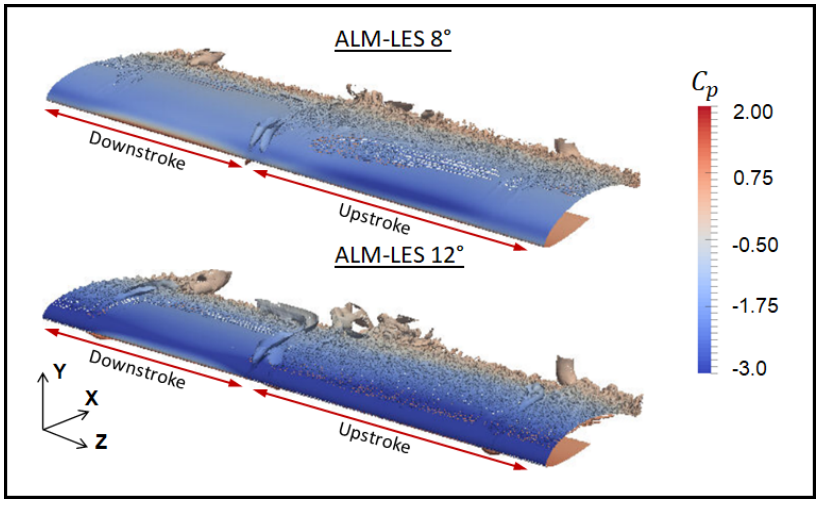

Fig. 6 Comparison of instantaneous on-wing vortical structures between ALM-LES 8° and 12° cases

Fig. 5 shows a similar comparison between the instantaneous views of the 12° case employing different turbulence

modeling approaches. Again, we use isosurfaces of Q-criterion colored by pressure to highlight the spanwise lift variation and vortical structures. While the asymmetry in rotor-related vorticity above and below the wing remains in all three approaches, the rotor-shed tip and root vortices persist further into the wake for the ALM-LES approach compared to the other turbulence modeling approaches which is likely related to the lower dissipation in the LES model. The ALM-LES approach also shows higher wing-related vorticity which interacts with the rotor vorticity in the wake of the rotor-wing system. The ALM-DDES approach shows qualitatively similar root and tip vortex evolution compared to ALM-LES although they do not persist as far into the wake. There is a visible roll-up of trailing edge shed vorticity in both the ALM-DDES and ALM-URANS approaches. While the ALM-DDES approach shows breakdown of these vortices later in the wake and their interaction with rotor vorticity, the ALM-URANS approach does not capture the complex 3D vorticity in the wing wake. Note that the mesh resolution in regions spanned by tip vortices is the same for the different turbulence modeling approaches considered.

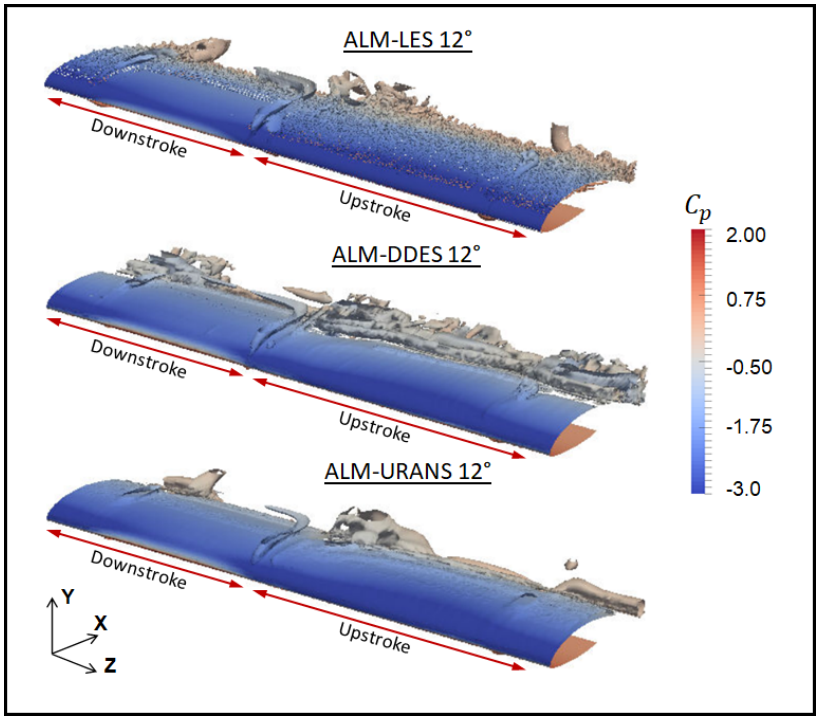

Fig. 7 Comparison of instantaneous on-wing vortical structures for 12° case with different turbulence models

In order to better observe the vortical structures on the wing surface, Fig. 6 shows the ALM-LES comparison between 8° and 12° cases with Q-criterion (colored by pressure) restricted to the vicinity of the wing. Fine-scale vortical structures can be observed on the wing surface in both AOAs which grow in size as they convect to the trailing edge in both cases. This indicates transition of the laminar boundary layer over the wing to turbulence as captured in LES. Both cases show spanwise variation in transitional behavior: the downstroke side shows a delay in transition due to the rotor-induced downwash, while the upstroke side shows earlier transition in both cases due to rotor-induced upwash. Qualitatively, the 12° case shows earlier transition, particularly on the upstroke side where the transition appears to start quite close to the leading edge.

Fig. 7 shows the 12° AOA comparison of on-wing vorticity employing different turbulence models. The ALM-DDES and ALM-URANS approaches do not capture the fine-scale vortical structures on the wing as observed in ALM-LES. This indicates lack of transition of the boundary layer to turbulence. The ALM-DDES approach shows a rapid transition in observed vorticity close to the trailing edge where the smooth laminar boundary layer separates and the vortex roll-ups from the wing break down in the wake. The upstroke side shows the separation earlier compared to the downstroke side. This separation is not observed in the ALM-LES approach where the transition to turbulence is expected to keep the boundary layer attached. The ALM-URANS approach shows the vortex roll-up from the trailing edge but the separation occurs later compared to the ALM-DDES approach and there is no visible breakdown of the shed vorticity.

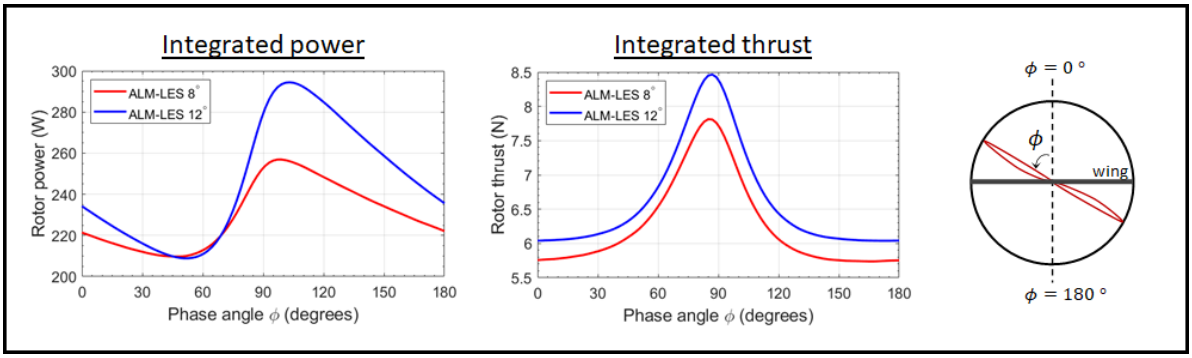

Fig. 8 Comparison of rotor power and thrust between ALM-LES 8° and 12° cases

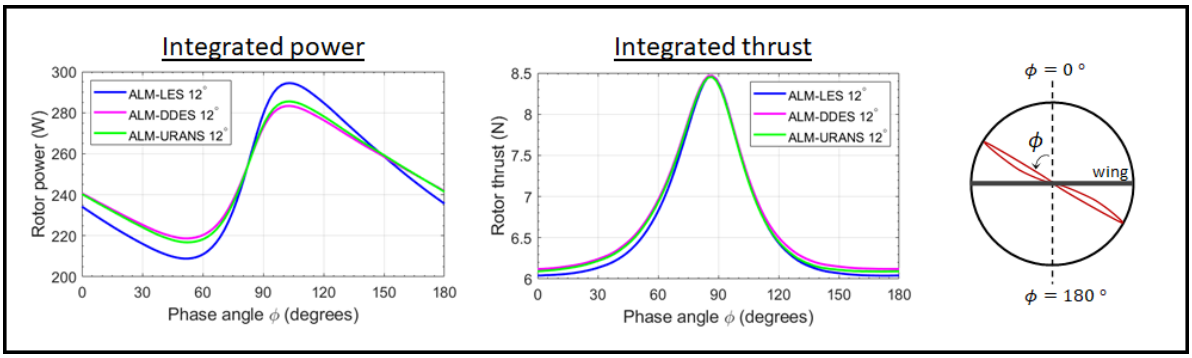

Fig. 9 Comparison of rotor power and thrust for 12° case with different turbulence models

B. Averaged Power, Thrust and Sectional Forces

Rotor (integrated) quantities are compared first. Fig. 8 shows a comparison of phase-averaged rotor power and thrust between the ALM-LES 8° and 12° cases. The phase-averaging is done over 5 revolutions of the rotor. For a symmetric two-bladed rotor, this corresponds to 10 samples collected for each phase in a cycle and therefore, phase-averaged data for half a cycle (i.e., up to 180° phase) is presented. The integrated power trends on the left panel show a marked difference between the two cases. While the power requirement is quite close between $\phi = 0°$ and $\phi = 90°$, the two curves start diverging beyond $\phi = 90°$ where rotor-wing interference is maximum. The 12° case shows a 14.52% increase in peak power compared to the 8° case, while the mean power required is 7.35% higher for the 12° case. The right panel shows the comparison of integrated thrust between the two angles of attack. Both cases show very similar trends in the thrust variation with the 12° case showing a nearly constant offset from the 8° case. Starting from the minimum thrust at $\phi = 0°$ (least rotor-wing interference), the thrust increases till the maximum thrust is encountered just before the $\phi = 90°$ position (greatest rotor-wing interference) after which it drops back down. The mean thrust over the cycle was 5.67% higher for the 12° case as compared to the 8° case.

Fig. 9 shows a comparison of phase-averaged rotor power and thrust for the 12° case employing different turbulence models. For the ALM-DDES and ALM-URANS approaches, the phase averaging is found to be sufficient over two revolutions of the rotor (corresponding to 4 samples for each phase in a cycle). The integrated power trends on the left panel show similar trends among the three approaches. The mean power required over the cycle for ALM-DDES and ALM-URANS approaches is within 5% of ALM-LES, however ALM-LES approach shows higher variation in power over the cycle. Peak-to-peak power for ALM-LES approach is $\sim$ 33.5% higher than peak-to-peak values for ALM-DDES and ALM-URANS approaches. The integrated thrust trends on the right panel are very close for the three approaches with ALM-DDES and ALM-URANS approaches showing mean and peak values within 2% of the corresponding ALM-LES predictions.

Next we compare sectional forces on the wing. Fig. 10 compares sectional lift between the ALM-LES 8° and 12° cases. The LES cases use 5 revolutions of time-averaging to obtain averaged forces over the span of the half-wing.

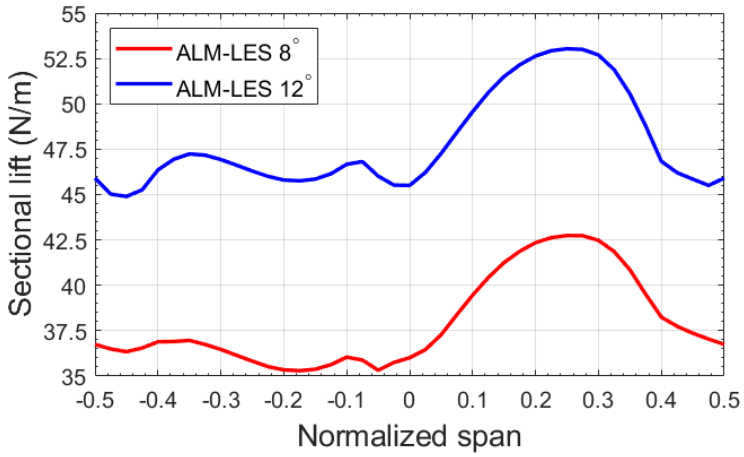

Fig. 10 Comparison of time-averaged sectional lift between ALM-LES 8° and 12° cases

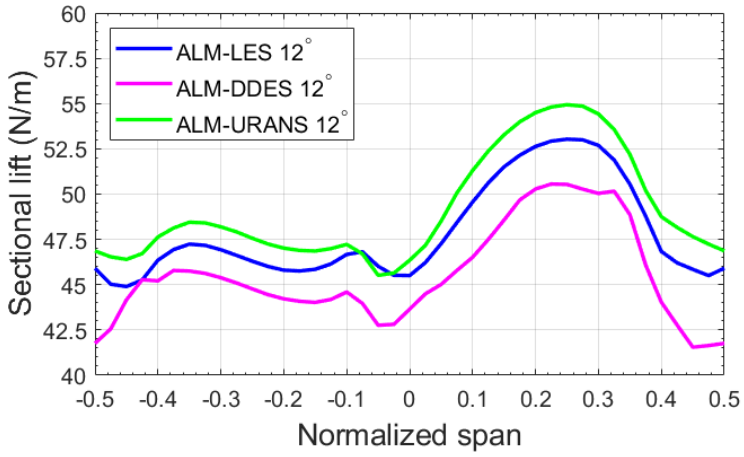

Fig. 11 Comparison of time-averaged sectional lift for 12° case with different turbulence models

The averaged sectional lift in the top panel clearly shows the spanwise variation in generated lift with a clear peak at ~ 30% of the half-span. The 12° case shows a 11.12% higher peak lift compared to its mean lift over the span while 8° shows a 12.63% higher peak lift compared to its mean lift. The downstroke side also shows a minor peak in both cases at ~ 35% of half-span due to the high dynamic pressure induced by the rotor despite the reduction in effective wing AOA. It is to be noted that the time-averaged lift on either end of the wing are identical due to the enforcement of the periodic condition in the span as discussed above. There is a clear separation between the two lift curves due to the change in AOA; the 12° case shows ~ 26% higher mean lift compared to the 8° case. Fig. 11 compares the sectional lift for the 12° case employing different turbulence models. As before, the ALM-DDES and ALM-URANS averaging uses two revolutions to obtain the averaged sectional forces. All three approaches show similar trends in the sectional lift with ALM-URANS showing the highest mean lift over the span, followed by ALM-LES and then ALM-DDES. ALM-URANS shows 2.80% higher mean lift compared to ALM-LES while ALM-DDES shows 4.66% lower mean lift compared to ALM-LES.

Finally, Fig. 12 compares time-averaged sectional pressure drag between the 8° and 12° ALM-LES cases. Both cases show clear peaks in pressure drag on the downstroke side. This is likely due to the induced downwash from the rotor shifting the stagnation point higher on the wing, this is visible in Fig. 6 where the downstroke side shows a high pressure region near the leading edge which is not visible on the upstroke side. The 12° case shows a 47% higher peak

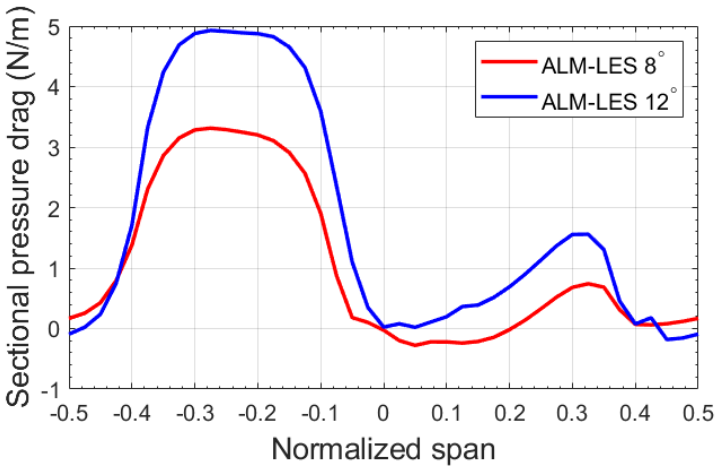

Fig. 12 Comparison of time-averaged sectional pressure drag between ALM-LES 8° and 12° cases

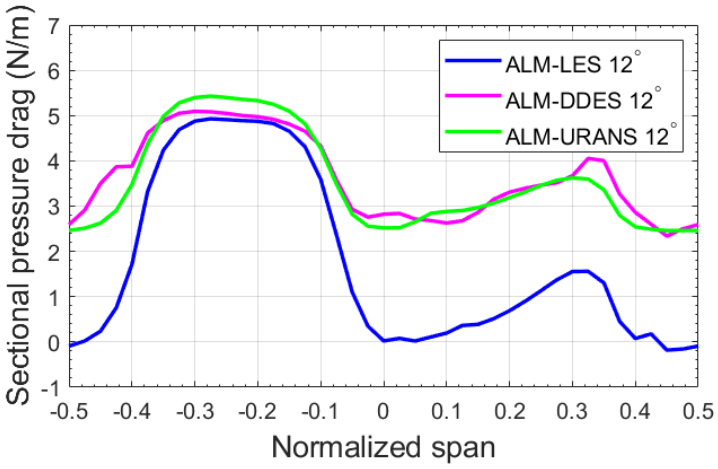

Fig. 13 Comparison of time-averaged sectional pressure drag for 12° case with different turbulence models

pressure drag compared to the 8° case on the downstroke side. The upstroke side also shows smaller peaks in drag for both cases while other sections show very low values of pressure drag. The mean pressure drag over the span for the 12° case is ~ 69% higher than the 8° case. Fig. 13 compares the sectional pressure drag for the 12° case employing different turbulence models. The ALM-DDES and ALM-URANS curves are quite close and show a clear difference from the ALM-LES curve. The pressure drag peaks on the downstroke side are quite close for all three approaches with ALM-URANS showing a ~ 10% higher value compared to ALM-DDES and ALM-LES while the rest of the span shows significantly higher pressure drag for the ALM-URANS and ALM-DDES approaches compared to ALM-LES. This is likely a result of flow separation observed earlier for the DDES and URANS approaches which is known to significantly increase the pressure drag. The mean pressure drag over the span for ALM-LES is observed to be ~ 51% lower than ALM-DDES and ALM-URANS predictions. The three different turbulence modeling approaches lead to significantly different predictions for pressure drag.

IV. Concluding Remarks

An infinite rotor-wing unit based on the CRC-20 quad-rotor bi-plane was modeled at two AOAs of 8° and 12° using different turbulence approaches including LES, DDES and URANS. The rotor was modeled using an ALM approach to

conserve cost while capturing key flow features. Instantaneous comparisons of vortical structures from the rotor-wing unit showed the ability of LES in capturing fine-scale vorticity on the wing indicating transition to turbulence which was absent in the ALM-DDES and ALM-URANS approaches. Spanwise variation was observed in the transition behavior on the wing in the ALM-LES approach with the 12° case showing higher vorticity as compared to the 8° case. The ALM-DDES and ALM-URANS approaches showed separation near the trailing edge which seems to be prevented in the ALM-LES approach due to transition to turbulence. The averaged rotor (integrated) thrust and power was found to be similar between the turbulence modeling appraoches although the ALM-LES approach showed $\sim 33.5\%$ higher peak-to-peak variation in power compared to ALM-DDES and ALM-URANS approaches. Averaged wing lift was found to be reasonably close between the three approaches while the averaged pressure drag was observed to be significantly different between the modeling approaches. The ALM-LES approach showed $\sim 51\%$ lower pressure drag compared to the ALM-DDES and ALM-URANS approaches.

In future, we plan to investigate in detail the differences observed among different turbulence modeling approaches, especially in pressure drag. We also plan to extend the infinite rotor-wing unit to a dual-propeller finite wing study and draw comparisons with isolated rotor and isolated wing cases with different turbulence modeling approaches.

References

[1] Singh, R., Sirohi, J., and Hrishikenvan, V., "Common Research Configuration for Collaborative Advancement of Scalable VTOL UAS Technologies," *75th Annual Forum of the American Helicopter Society*, 2019.

[2] Aref, P., Ghoreyshi, M., Jirasek, A., Satchell, M., and Bergeron, K., "Comp. Study of Prop.–Wing Aero. Interaction," *Aerospace*, Vol. 5, 2018, p. 79.

[3] Fischer, J., and Ortun, B., "Simulation & analysis of the aerodynamic interaction between distributed propulsion and wings," *AHS Technical Meeting on Aeromechanics Design for Transformative Vertical Flight*, 2018.

[4] Misiorowski, M., Gandhi, F., and A-Inthra, P., "Comp. Analysis of Rotor-Blown-Wing for Elec. Rotorcraft Apps." *AIAA J.*, 2020.

[5] Stokkermans, T. C., van Arnhem, N., Sinnige, T., and Veldhuis, L. L., "Validation and comparison of RANS propeller modeling methods for tip-mounted applications," *AIAA Journal*, Vol. 57, 2019, pp. 566–580.

[6] Sinnige, T., van Arnhem, N., Stokkermans, T. C., Eitelberg, G., and Veldhuis, L. L., "Wingtip-Mounted Propellers: Aerodynamic Analysis of Interaction Effects and Comparison with Conventional Layout," *J. of Aircraft*, Vol. 56, 2019, pp. 295–312.

[7] van Arnhem, N., de Vries, R., Vos, R., and Veldhuis, L. L., "Aerodynamic Performance of an Aircraft Equipped with Horizontal Tail Mounted Propellers," *AIAA Aviation 2019 Forum*, 2019.

[8] Conley, S., Russell, C., Kallstrom, K., Koning, W., and Romander, E., "Comparing RotCFD Predictions of the Multirotor Test Bed with Experimental Results," *VFS 76th Annual Forum*, 2020.

[9] McGlynn, E., Tran, S., and Sahni, O., "LES of Flow Interactions of Seg. Synthetic Jets on an Airfoil," *AIAA FD Conf.*, 2017.

[10] Rane, J., and Sahni, O., "LES of surging airfoils at high adv. ratio and Reynolds number," *AIAA Applied Aero. Conf.*, 2018.

[11] Tran, S., and Sahni, O., "FE-based LES using a comb. of VMS and dynamic Smag. model," *J. of Turb.*, Vol. 18, 2017, pp. 391–417.

[12] Russell, C., and Sekula, M., "Comprehensive analysis modeling of small-scale UAS rotors," *VFS 76th Annual Forum*, 2020.

[13] Niemiec, R., and Gandhi, F., "Development and Validation of the Rensselaer Multicopter Analysis Code (RMAC): A Physics-Based Comprehensive Modeling Tool," *75th Annual Forum of the American Helicopter Society*, 2019.

[14] Hebbar, U., Rane, J. D., Gandhi, F., and Sahni, O., "Analysis of Interactional Aerodynamics in Multi-Rotor Wind Turbines using Large Eddy Simulations," *AIAA Scitech 2020 Forum*, 2020, p. 1489.